ELSEVIER

Chemical Geology 229 (2006) 144–161

CHEMICAL GEOLOGY
INCLUDING
ISOTOPE GEOSCIENCE

www.elsevier.com/locate/chemgeo

Structural environment of iron in hydrous aluminosilicate glass and melt-evidence from X-ray absorption spectroscopy

Max Wilke [a,*], Christian Schmidt [b], Francois Farges [c], Valerie Malavergne [c], Laurent Gautron [c], Alexandre Simionovici [d], Matthias Hahn [e], Pierre-Emanuel Petit [f]

[a] *Institut für Geowissenschaften, Universität Potsdam, 14415 Potsdam, Germany*
[b] *GeoForschungsZentrum Potsdam, 14473 Potsdam, Germany*
[c] *Laboratoire des Géomateriaux, Universite Marne-la-Vallée, 77454 Marne la Vallée cedex 2, France*
[d] *Laboratoire des Sciences de la Terre, ENS Lyon, 69007, Lyon, France*
[e] *Institut für Mineralogie, Universität Hannover, 30167 Hannover, Germany*
[f] *UMR 06502 Institut des Materiaux Jean Rouxel-EPUN, 44322 Nantes Cedex 3, France*

Accepted 6 January 2006

Abstract

The iron speciation in hydrous haplotonalitic and haplogranitic silicate glasses was studied using XAFS spectroscopy and transmission electron microscopy (TEM). Spectral features occurring at the main crest of the XANES at the iron K-edge of hydrous glasses indicate contributions to the spectra by iron-moieties present in a more ordered structural environment than found in the dry glass. These differences are also suggested by analysis of the EXAFS. These effects are not completely suppressed even for those samples that were quenched with a higher cooling rate. Strongest differences to the dry glass are observed for a sample that was quenched slowly through the temperature of glass transformation. Crystals (60 to 1500 nm in size) of magnetite, maghemite and another unidentified phase were observed in this sample by TEM, whereas no crystals were found in samples quenched with regular or high cooling rates. In-situ XANES measurements up to 700 °C and 500 MPa were performed to reveal the origin (i.e., during synthesis or quench) of the structural differences for those hydrous glasses that do not display any detectable crystallization. The comparison of XANES spectra collected on Fe^{2+} in water-saturated haplogranitic melt at 700 °C and 500 MPa and on Fe^{2+} in dry melt at 1150 °C shows that the local structural environment of Fe^{2+} in both systems is similar. This indicates that there is no detectable and direct influence of water on the local structure around iron in this type of melt. Hence, the differences observed between hydrous and dry glasses can only be related to artefacts formed during the quench process.

1. Introduction

Due to its ubiquitous abundance on Earth and its heterovalent nature in molten silicates, iron plays a significant role in many magmatic processes. In particular, the heterovalency of iron has a large effect on the evolution of magmas during melting and crystallization. Because Fe^{3+} and Fe^{2+} can occur in a variety of different structural environments, physical and chemical properties of magmas are often strongly dependent on the oxidation state of iron (e.g., Mysen, 1991). Although the oxidation state is mostly controlled by oxygen fugacity (fO_2), both oxidation state and coordination are also functions of melt composition, volatile content, temperature and other parameters (e.g.,

* Corresponding author. Tel.: +49 331 977 2483; fax: +49 331 977 5060.
E-mail address: max@geo.uni-potsdam.de (M. Wilke).

0009-2541/$ - see front matter © 2006 Elsevier B.V. All rights reserved.
doi:10.1016/j.chemgeo.2006.01.017

Johnston, 1964, 1965; Fudali, 1965; Sack et al., 1980; Kilinc et al., 1983; Dyar, 1985; Mysen et al., 1985; Paul, 1990; Borisov and Shapkin, 1990; Kress and Carmichael, 1991; Moore et al., 1995; Baker and Rutherford, 1996; Burkhard, 2000; Gaillard et al., 2001; Wilke et al., 2002; Botcharnikov et al., 2005). Addition of volatile components (such as H_2O, CO_2 and CH_4) to silicate melts directly influences the prevailing oxygen fugacity and, therefore, affects the redox state of the melt by internal buffering reactions, e.g., $H_2+1/2\ O_2=H_2O$ or $CO+1/2\ O_2=CO_2$ (e.g., Holloway and Blank, 1994). Moreover, addition of volatiles considerably changes the bulk structure of the melt (e.g., Mysen and Virgo, 1986; Kohn et al., 1989; Zotov et al., 1992; Kohn, 2000). The exact mechanism of the incorporation of water in silicate melts is not yet fully understood but appears to be strongly dependent on melt composition. In hydrous alkali-silicate glasses, there is NMR and Raman spectroscopic evidence for the formation of non-bridging oxygens (e.g., Kümmerlen et al., 1992; Zotov and Keppler, 1998; Xue and Kanzaki, 2004). In contrast, no formation of non-bridging oxygens was found in hydrous aluminosilicate compositions (e.g., Kohn et al., 1989; Schmidt et al., 2000), whereas significant changes were observed in the environment of sodium (Kohn et al., 1998). These changes in the structure upon dissolution of water in the melt may also potentially affect the structural environment of iron.

In a previous study, we investigated the relationship between iron-oxidation state and fO_2 at 500 MPa water pressure based on Mössbauer spectroscopy of quenched melts (Wilke et al., 2002). While determination of the iron-oxidation state from numerical fits of the Mössbauer spectra yielded reliable results, quantitative determination of the local structure around iron in these glasses was not possible. This was due to the strong line broadening caused by site-to-site distribution of the iron coordination environment. However, distribution analysis of the hyperfine parameters showed that the distributions of Fe^{3+} and Fe^{2+} strongly overlap in case of dry glass, in contrast to a much clearer separation of the distributions for the hydrous glasses. This difference in the hyperfine parameter distribution indicated that the structural units of Fe^{3+} and Fe^{2+} in these hydrous glasses are more distinct and probably less variable, but did not necessarily imply a change in the iron coordination of the water-bearing glasses. An increase of the quench rate from 150–100 K/min to >150 K/s did not change the observed hyperfine parameter distribution. In contrast, a slow cooling rate (1 K/min) through the glass transformation temperature T_g (250–350 °C) resulted in a considerably smaller hyperfine parameter distribution, which indicated the onset of crystallization.

Here, we use X-ray absorption fine structure (XAFS) spectroscopy at the iron K-edge to further constrain the differences between dry and hydrous glass observed by Mössbauer analysis. XAFS is sensitive to the oxidation state, especially the pre-edge feature, located ~15–20 eV before the main K-edge crest of iron (e.g., Waychunas et al., 1983; Calas and Petiau, 1983; Bajt et al., 1994; Galoisy et al., 2001; Wilke et al., 2001; Berry et al., 2003; Wilke et al., 2004a,b; Farges et al., 2004; Jackson et al., 2005). XAFS provides structural information on the nearest and next-nearest neighboring atoms around iron. Although XAFS is a method often used for structural analysis in systems lacking long-range order, it is highly sensitive to structural changes in relation to nucleation or ordering processes around the atom of interest (Farges et al., 2001). Combined with transmission electron microscopy (TEM), XAFS is an ideal tool to further investigate the differences between dry and hydrous glasses. The interpretation of the obtained spectra is based on an extensive study on model compounds to comprehensively understand the spectral changes with oxidation state and structural environment of the absorbing iron atom (Wilke et al., 2001). The applicability of these results from that study was validated thanks to a variety of other methods such as ab-initio models of the pre-edge and XANES features (Farges et al., 2005), magnetic circular dichroism (Jackson et al., 2005) and molecular dynamics (Farges et al., 2004). In this study, transmission electron microscopy was used to detect and characterize crystals that may have formed in the glasses during the synthesis or quench and that could not be visualized by other methods.

In addition to the better characterization of the structural environment of iron in the dry and hydrous glasses by XAFS, we conducted XAFS measurements at in-situ conditions (high temperature, HT, and high temperature/high pressure, HT/HP) to provide unambiguous information whether these structural differences originated during synthesis at pressure and temperature or at temperatures around T_g during the quench. These in-situ investigations were performed using a hydrothermal diamond anvil cell (HDAC) that was optimized for XAFS measurements at the iron K-edge.

2. Experimental

2.1. XAFS data collection on glasses

XAFS spectra at the iron K-edge were collected at the European Synchrotron Radiation Facility (ESRF,

Grenoble, France), on the undulator beamline ID26 (Gauthier et al., 1999; Solé et al., 1999), at HASYLAB (Hamburg, Germany) on beamline A1 and at the SSRL (Stanford, USA) on beamline 11-2. At the ESRF, the storage ring operating conditions were 6 GeV electron energy and 150–185 mA electron current. A Si(220) double-crystal monochromator was used for acquisition of high-resolution XANES scans. Two mirrors were used to remove the high-energy harmonics from the incident X-ray beam (cutoff energy at 10 keV). At HASYLAB, EXAFS spectra were recorded using a channel-cut Si(111) double-crystal monochromator with the positron storage ring operating at 4.5 GeV and 70–120 mA. High-energy harmonics were rejected by detuning of the second crystal (intensity was reduced by 40%). At the SSRL, the XANES and EXAFS spectra were recorded using a Si(220) double-crystal monochromator with the SPEAR2 storage ring operating at 3 GeV and 30–100 mA. High-energy harmonics were rejected by detuning of the second crystal (intensity was reduced by 40%). The XAFS data were collected in fluorescence mode with the sample positioned in a 45° angle to the beam. The fluorescence yield was measured as a function of X-ray energy using a pin-diode detector (ESRF) or a Stern-Heald-type detector (Lytle et al., 1984) filled with Kr (SSRL). A MnO filter (3 μ absorbance) was used to minimize unwanted elastic scattering. At HASYLAB, a five-element high purity Ge detector was used. For all experiments, a reference sample (usually metallic iron) was used to provide an internal and accurate energy calibration of the monochromator (first inflection point of the iron K-edge set at 7111.08 eV). The energy reproducibility for these experiments is ±0.05 eV.

XANES spectra at all beamlines were collected from ~50 eV below to 200 eV above the iron K-edge (7050–7300 eV), with 0.1 eV steps for the pre-edge region (7108–7116 eV). The XANES spectra were normalized in absorbance by fitting the spectral region from 7050 to 7090 eV (the region before the pre-edge) using a polynomial and subtracting this as background absorption. The spectra were then normalized for atomic absorption, based on the average absorption coefficient of the spectral region from 7200 to 7300 eV (i.e., after the edge crest). The pre-edge of the spectra taken on glass and melt was modeled by fitting two Gaussian functions for the pre-edge peaks and two further Gaussian functions to model the contribution of the main edge to the pre-edge background using a part of the spectra between 7104 and 7118 eV. Pre-edge peaks of glasses are more broadened compared to pre-edges from crystalline model compounds (Wilke et al., 2001), which is due to the less defined site geometry in glasses (Rossano et al., 2000). In addition, especially in glasses containing both oxidation states, parts of the pre-edge peaks related to ferrous iron overlap with those of ferric iron, which cannot be resolved by numerical fitting. Thus, the use of two Gaussians to describe the pre-edge in glasses represents the approach with a minimum number of fit parameters. This approach was successfully used to derive the oxidation state on a series of glasses with known oxidation state (Wilke et al., 2004a, b). In addition to this, Farges et al. (2004) have shown that using two components for modeling the pre-edge and the use of a variogram as suggested by Wilke et al. (2001) is a robust way to derive iron-oxidation state and symmetry information from the pre-edge. It should be noted here, that the pre-edge intensity only probes the site geometry of a given element, i.e., the presence of a center of symmetry in the coordination polyhedron. An assignment to the symmetry of coordination polyhedra is derived from comparison to pre-edges of model compounds and only an average coordination symmetry is estimated. Strictly speaking, the assignment of an average coordination requires additional information, e.g., from the first EXAFS oscillation in the main edge spectra. However, in silicate glasses, only four-, five- and six-coordinated environments were unambiguously detected (Jackson et al., 1993, 2005), making a coordination assignment "possible" that is based only on pre-edge information. The "average" pre-edge information was obtained by calculating the "total integrated area" and its centroid (area-weighted average of the pre-edge peak position). These two parameters were calculated directly from the fitted pre-edge peaks.

EXAFS spectra were collected up to 650 eV after the edge (k=13 Å^{-1}, k being the photo electron wave vector in atomic units). Spectra of all samples were collected at room temperature. In addition, a suite of selected samples were collected at 77 K using a cryostat with liquid nitrogen in order to suppress contributions to the spectra from thermally induced disorder. EXAFS spectra were analyzed using the XAFS program (version 2.9) by Winterer (1996). The edge position E_0 was determined using the inflection point of an error function fit to the edge jump. Normalization after the edge was performed using a cubic spline function for subtraction of background and low-frequency noise from the EXAFS oscillations. The normalized EXAFS oscillations, $\chi(k)$, were k^3-weighted and Fourier-transformed by using a Kaiser-Bessel filter.

2.2. In-situ XANES using the hydrothermal diamond anvil cell

The in-situ measurements were conducted using a Bassett-type HDAC (Basset et al., 1993), which was optimized to acquire XANES spectra at the iron K-edge. The spectra were collected in fluorescence mode. This was done because a rather low iron concentration was used to avoid precipitation of iron-bearing phases in the melts during the experiments. To minimize the absorption of the incident X-ray beam and to collect the fluorescence signal at 90° to the incident beam, we combined modifications of the cell design described by Schmidt and Rickers (2003) and Basset et al. (2000). Recording of the fluorescence signal at 90° minimizes the background in the spectra from elastic and Compton scattering. To make measurements in this geometry feasible, a 60 μm deep and 300 μm wide recess was drilled in the culet face of the anvil that is located at the side of the incident beam (Fig. 1A). Essentially, only fluorescence X-rays generated in the recess volume can reach the detector. In addition, a second conical recess,

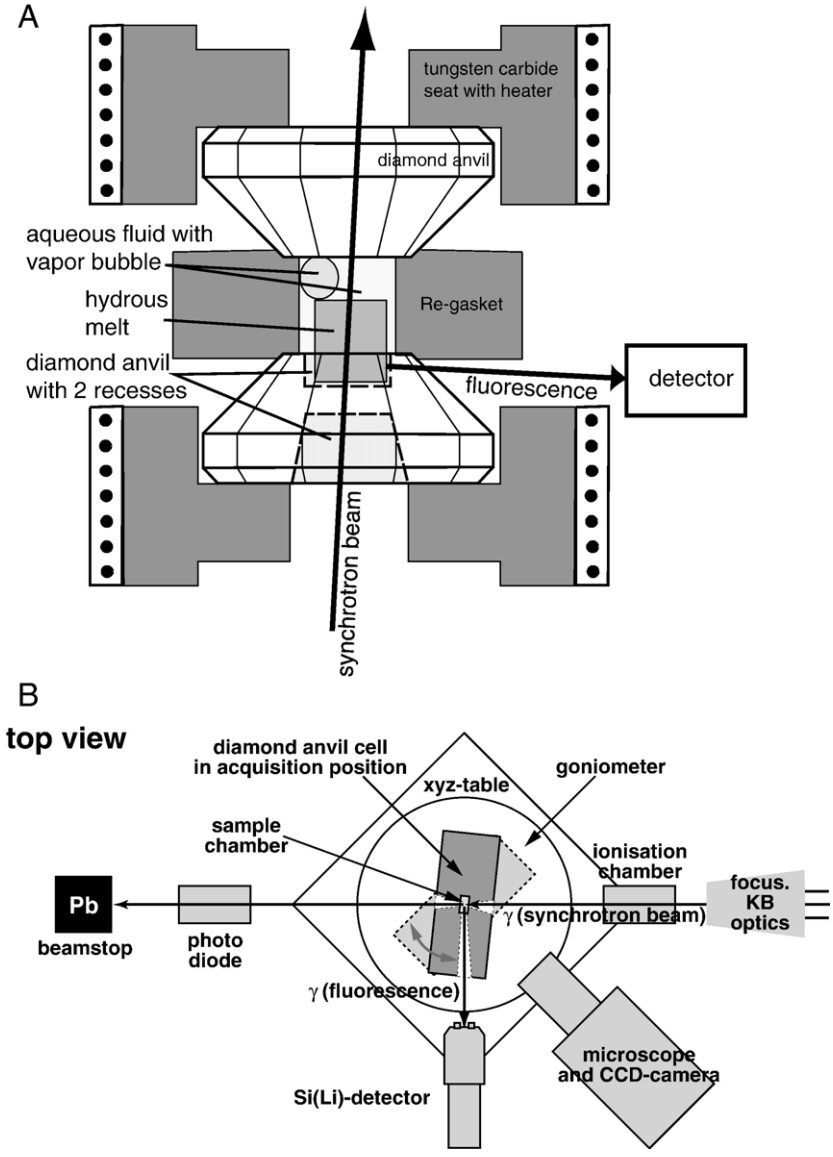

Fig. 1. (A) Schematic diagram showing the details of the modified diamond anvil cell. To minimize absorption of X-rays by the diamond and to enable acquisition of spectra in fluorescence mode, recesses were drilled in the culet and back face of the front anvil. (B) Top view of the setup configuration for the experiment at beamline ID 22, ESRF.

about 1.5 mm in depth, was drilled into the table face of the anvil, which reduced the path length of the incident beam through the diamond to about 440 μm (Fig. 1A). The path length of the fluorescence signal through the diamond is about 350–450 μm.

The cell was heated externally by NiCr coils around the tungsten carbide seats, which support the anvils. The temperature was recorded by K-type thermocouples that are attached to the diamonds. The temperature was controlled within ±0.5 °C of the set value using a Eurotherm 2704 controller. The temperature in the sample chamber was calibrated using the melting points at ambient pressure of sodium chloride (800.5 °C) and sodium nitrate (306.8 °C). Temperature differences between thermocouples and sample chamber were found to be below 4 °C. The Re gasket had a thickness of 125 μm and a hole diameter of 350 μm. Cylinders of water-bearing glass were placed inside the sample volume after mounting the gasket on the lower anvil. Water was then added to serve as pressure medium. An air bubble was present when the cell was sealed and the volume ratio of water to bubble was chosen to reach pressures around 500 MPa at 700 °C. The loaded cell was mounted on the sample XYZ-stage at the beamline. Optical observation of the sample chamber of the cell using a microscope was possible after the cell was turned around the *Z*-axis by 45° from the measurement position. After the desired temperature was reached, the cell was aligned with the beam and the fluorescence detector. The pressure at the experimental temperature was calculated using an equation of state of water (Haar et al., 1984) based on the liquid–vapor homogenization temperature of the aqueous fluid measured after spectrum acquisition at HP/HT.

The in-situ HP/HT XANES spectra were collected at the ESRF at the micro-focus beamline ID22. A Si(111) double-crystal monochromator was used for these experiments to obtain as much flux on the sample as possible. The spectra were collected in fluorescence mode using an energy dispersive Si(Li) solid state detector with 30 mm^2 active area. Higher harmonics in the incident beam were rejected using a Si mirror (cutoff 12 keV). The beam was focused at the experiment using a Kirkpatrick-Baez mirror (KB) system that provided a spot size of 4.5 × 6 μm at 17.5 keV for the chosen setup. The incident beam intensity was measured using an N_2-filled ionization chamber between the KB optics and the pressure cell. For alignment, the beam intensity behind the cell was monitored using a photo diode. XANES spectra were acquired and processed as described for the measurements on glasses.

2.3. Transmission electron microscopy (TEM)

The glass samples were mounted in epoxy resin, sectioned and polished in order to obtain thin slides. They were then mounted on 3 mm Cu rings with central single holes 600 μm in diameter and then thinned until perforation of the samples using an argon-ion beam with a voltage of 4 kV and currents of 0.5 mA on each cathode. They were finally coated with a thin film of carbon, to prevent sample charge effects. The samples were studied using a JEOL 2000 EX Transmission Electron Microscope operating at 200 kV equipped with a Tracor TN 5400 FX X-ray analyzer, which provided energy-dispersive X-ray analyses (EDX). The micro-analyses were carried out in scanning transmission mode with live times ranging between 30 and 100 s and 8000 to 15,000 net counts for the major elements. K-factors for Si, Mg and Fe were determined from measurements of the elemental ratios in olivine and pyroxene standards at different thicknesses and subsequent extrapolation of the ratios to zero thickness. These calibrations ensure an accuracy of the determined chemical compositions of 5% (e.g., Malavergne et al., 1999).

2.4. Synthesis of glass samples

2.4.1. Haplotonalitic samples

We have studied a suite of synthetic glasses of haplotonalitic composition ($Qz_{48}Ab_{22}An_{30}$: Qz—SiO_2, Ab—$NaAlSi_3O_8$, An—$CaAl_2Si_2O_8$), which was previously characterized using Mössbauer spectroscopy (Wilke et al., 2002). The compositions of these glasses are reported in Table 1. Their Fe_2O_3 content is about 1.5 wt.%. The hydrous glasses were equilibrated at 500 MPa and 850 °C at water-saturated

Table 1
Average composition (in wt.%) and CIPW normative compositions of dry starting glasses (standard deviation given in parentheses)

	Haplogranite	Haplotonalite
SiO_2	76.2(3)	76.1(9)
Al_2O_3	12.5(3)	14.50(9)
CaO	n.d.	6.0(6)
K_2O	3.6(1)	n.d.
Na_2O	5.1(1)	2.6(1)
Fe_2O_3 (tot.)	1.4(1)	1.6(1)
Total	100.4	100.8
Qz	33.6	48.5
Ab	44.5	21.7
Or	21.7	
An		29.8
C	0.2	0.0

n.d.: not determined.

conditions (12 wt.% total water content). Presence of free water in the sample capsules after the run indicated water-saturated conditions for all runs. The glasses contain about 11 wt.% water after the synthesis (determined by Karl-Fischer Titration, see Wilke and Behrens, 1999; Wilke et al., 2002). A detailed description of the synthesis procedure of the dry and hydrous glasses is given in Wilke et al. (2002). In addition to syntheses of hydrous glass using the normal quench routine in the internally heated pressure vessel, additional syntheses were performed with higher and lower quench rates to study the effect of cooling history on the iron-species. The quench rate for the normal quench is ca. 150 K/min above 500 °C and ca. 100 K/min below 500 °C (Wilke et al., 2002). The fast quench was performed by dropping the sample from the hot spot to the cool part of the gas pressure vessel resulting in quench rates of ca. >150 K/s. A slow quench was done by cooling the sample with the normal rate down to 360 °C followed by slow cooling through T_g down to room temperature (1 K/min). T_g is estimated to be 250–350 °C for the hydrous melt, based on viscosity data (Schulze, 2000).

2.4.2. Haplogranitic samples

The haplotonalitic composition was not suitable to study the iron species in hydrous melt at in-situ conditions, because the liquidus is located at temperatures that are above the temperature at which the HDAC can be operated for a couple of hours without frosting the diamond surfaces (about 800 °C). Therefore, a haplogranitic composition $Qz_{33}Ab_{45}Or_{22}$ (Or—$KAlSi_3O_8$) was used. Likewise, about 1.5 wt.% Fe_2O_3 was added to the base composition. The iron-free composition used here corresponds to the eutectic composition at 500 MPa water pressure (Holtz et al., 1992), which is completely molten above 650 °C at this pressure. The dry starting glasses were synthesized at 1600 °C in air as described in Wilke et al. (2002); the hydrous glasses were equilibrated at 500 MPa and 1100 °C at water-saturated conditions (12% total water content). About 11 wt.% of water are dissolved in the glass after the synthesis (Holtz et al., 1995). In addition to the water-saturated glass used for the in-situ measurements, also a hydrous glass with 4 wt.% water was synthesized.

3. Results and discussion

3.1. XANES of glasses

3.1.1. Haplotonalitic samples

Iron K-edge XANES spectra of the haplotonalitic glasses are shown in Fig. 2A and B. The comparison of the XANES spectra of dry and hydrous glasses indicates differences in the structural environment around iron, which is consistent with previous observations made by Mössbauer spectroscopy (Wilke et al., 2002). The hydrous glasses show higher intensities at the main-edge maximum (Fig. 2A, position A). The differences to the dry glass vary in intensity between fast and regularly quenched glasses synthesized at the same redox conditions (NNO+2.7, Fig. 2B). However, they also vary slightly among the regularly quenched samples, where they are strongest for the most oxidized sample (NNO+5.1, Fig. 2A). A pronounced maximum at position B is visible only in the slowly quenched sample (Fig. 2B). Finally, the first EXAFS maximum (position C) is shifted to lower energies for all hydrous glasses in comparison to the dry glass (Fig. 2A).

Higher intensities at the main-edge maximum (position A) may be related to an increase of the iron coordination number or to a decrease in the static disorder of the nearest neighbors (Farges et al., 2001). The variation of the spectral differences may reflect slight differences in the actual cooling rate of the regularly quenched samples. In any case, the rapidly quenched sample appears to show the weakest effects. The slowly quenched sample shows the strongest intensity increase at position A and, furthermore, a substantial narrowing of the peak and a fine structure that is not present in the other hydrous samples. The appearance of a maximum at position B can be explained by either the presence of more regular and aligned environments promoting multiple-scattering features or the presence of strongly backscattering neighbors (such as iron second neighbors) in a more ordered medium-range environment of iron (Farges et al., 2001). This and particularly the feature at position B may indicate onset of crystallization (see also TEM results). The shift in the first EXAFS maximum can be caused by an increase of the Fe–O distance or a change in the oxidation state. The latter can be ruled out as the only factor in case of the hydrous glasses studied here, because all samples show this shift, even those that are comparable in iron oxidation state to the dry sample (Table 2). Therefore, the energy shift of the first EXAFS maximum is probably related to an increase of the Fe–O distance, which would be consistent with an increase of the iron coordination number.

3.1.2. Haplogranitic samples

XANES spectra and fitted pre-edges of the haplogranitic glasses are shown in Fig. 2C. Comparison of the spectra taken on the hydrous glasses to the one of the dry glass also reveals some differences. Particularly, the water-saturated sample shows some increase in the

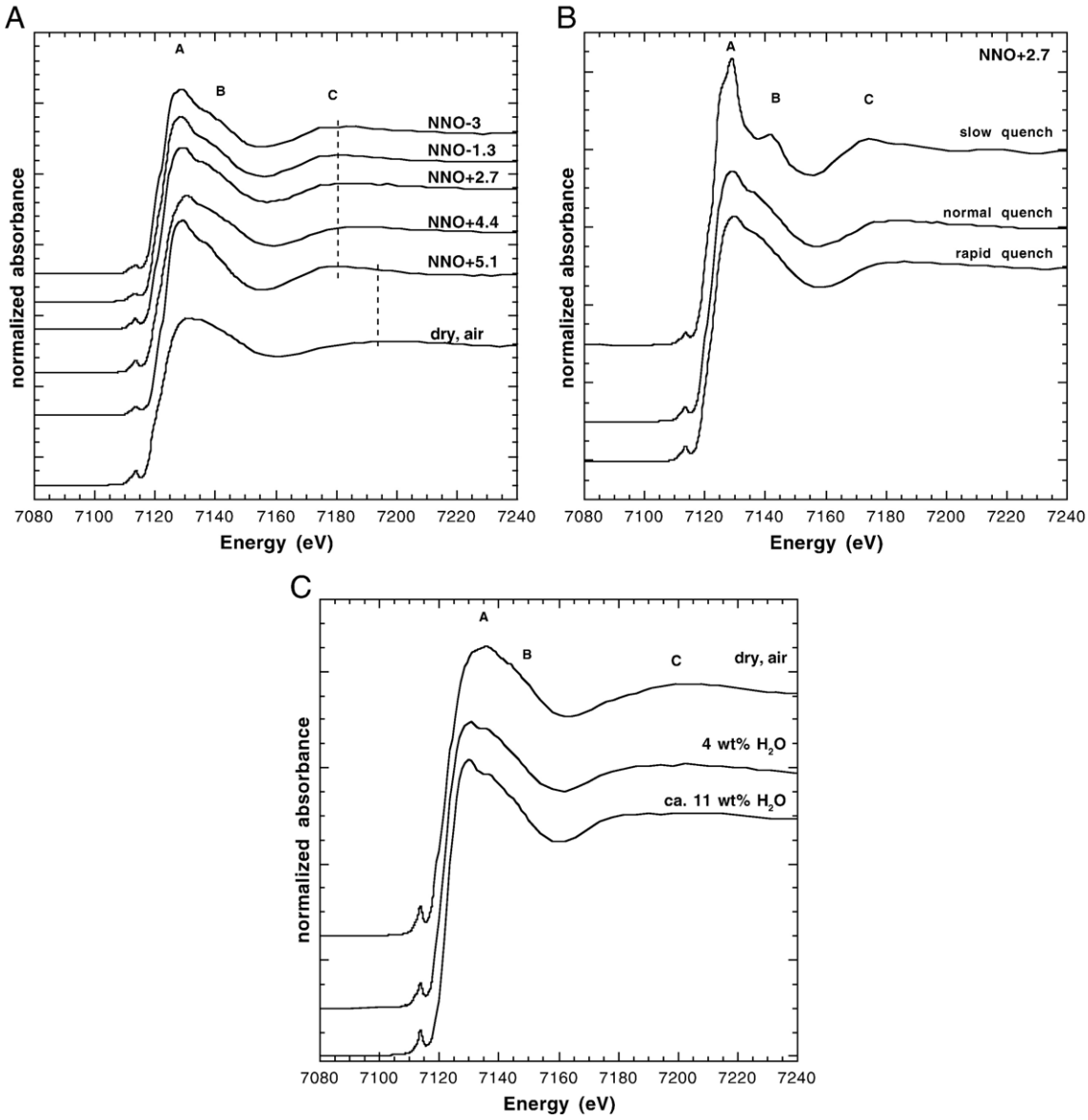

Fig. 2. XANES spectra at Fe K-edge of dry and hydrous iron-bearing haplotonalitic glasses. (A) Samples synthesized at redox conditions indicated (quenched using the normal quench rate). The dry sample was equilibrated in air at 1600 °C, 1 atm. Hydrous samples were equilibrated at 850 °C, 500 MPa water pressure (12 wt.% total water content). (B) Samples synthesized at intrinsic redox conditions (NNO+2.7) but quenched with different quench rates (all other parameters as in a). (C) XANES spectra of dry and hydrous iron-bearing haplogranitic glasses. The dry sample was equilibrated in air at 1600 °C, 1 atm. Hydrous samples were equilibrated at 1100 °C, 500 MPa, intrinsic redox conditions and total water contents indicated. Sample with 11 wt.% water content corresponds to water-saturated conditions.

feature A, whereas a shoulder at position B is not apparent. A slight shift of the maximum at position C towards lower energies is observed for the hydrous samples.

The differences at the main edge are quite similar to those observed for the haplotonalitic glasses and thus indicate some similarity in the difference of the local structural environment of iron in these two compositions. Again, the difference at position C between hydrous and dry glass may indicate some change in the Fe–O distance or difference in oxidation state as discussed for the haplotonalitic samples.

3.2. Pre-edge analysis

The fitted pre-edges of the spectra (Fig. 3A to C) are composed of two overlapping contributions one at lower

Table 2
Pre-edge parameters determined on the spectra taken on glasses

Sample, fO_2	Integrated intensity	Centroid pos. (eV)	$Fe^{3+}/\sum Fe$ from Wilke et al. (2002)
	±5% rel.	±0.05	±0.07
Haplotonalite			
Dry, 1 atm (air)	0.1812	7112.98	0.36
Hydrous, NNO+5.1	0.0970	7113.15	0.43
Hydrous, NNO+4.4	0.1423	7113.05	0.23
Hydrous, NNO+2.7, SQ	0.1024	7113.01	0.24
Hydrous, NNO+2.7, NQ	0.1279	7112.91	0.20
Hydrous, NNO+2.7, RQ	0.1311	7113.01	0.23
Hydrous, NNO−1.3	0.1118	7112.82	<0.04
Hydrous, NNO−3.0	0.1121	7112.77	l.d.
Haplogranite			
Dry, 1 atm (air)	0.1855	7113.10	n.d.
Hydrous	0.1534	7113.26	n.d.
Hydrous 4 wt.% water	0.1571	7113.00	n.d.

SQ: slow quench, NQ: regular quench, RQ: rapid quench, l.d.: below detection limit.
NNO: nickel–nickel oxide buffer.
Unless specified, samples were synthesized at 500 MPa at water-saturated conditions. Dry samples were synthesized at 1600 °C, hydrous haplotonalitic samples at 850 °C and hydrous haplogranitic samples at 1100 °C.

energies dominantly from Fe^{2+} and one at higher energies more related to Fe^{3+} as described earlier (e.g., Galoisy et al., 2001; Bonnin-Mosbah et al., 2001; Wilke et al., 2004a,b; Farges et al., 2004). Changes in the relative intensity of the two contributions are related to differences in the oxidation state of the samples, but may also be affected by changes in the symmetry. The integrated intensity and the centroid position of the pre-edges, derived from the fits of the pre-edge, are shown in Fig. 4 in comparison to those of Fe^{2+} and Fe^{3+} in various site geometries of model compounds (taken from Wilke et al., 2001, 2004). Based on molecular dynamics simulations (Rossano et al., 2001; Farges et al., 2004) and Magnetic Circular Dichroismen measurements (Jackson et al., 2005), no other geometries than T_d, C_{3h} and O_h are likely to be encountered in glasses and melts.

The differences in the centroid position of the pre-edges are mainly related to differences in the iron oxidation state depending on the $f(O_2)$ during the syntheses. Most of the hydrous *haplotonalitic* samples, except two, plot along a sub-linear trend in the field between the ferrous and ferric end-members. The dry sample has a higher intensity than the trend defined by the hydrous samples. The two samples, which do not plot on the above-mentioned trend of the other hydrous haplotonalitic samples, are the one synthesized at the most oxidizing conditions and the one that was slowly quenched.

Both water-bearing *haplogranitic* samples have similar pre-edge intensities, which are lower than the one of the dry sample (Fig. 4). The water-saturated sample shows a significantly higher centroid position than the dry sample and plots at a position that would be consistent with the trend defined by the haplotonalitic samples. In contrast, the sample under-saturated in water shows a lower centroid position. The fact that the two hydrous haplogranitic samples differ in the centroid position (and thus Fe^{3+}-content), although they were both synthesized at intrinsic conditions, is related to the difference in total water content, as the $f(O_2)$ prevailing in the sample capsule during the synthesis depends on the water activity (see also Botcharnikov et al., 2005).

Assignment of iron coordination based on the pre-edge data alone is uncertain as explained above and due to the possible presence of a mixture of up to four iron species in silicate glass (Brown et al., 1995). E.g., no differences can be made in this approach between a mixture of tetrahedral and octahedral coordination and a pure trigonal-pyramidal coordination as both can have the same pre-edge intensity and centroid position, so that only an idea of the average coordination can be developed.

An extrapolation of the trend, indicated by the dashed line in Fig. 4, to potential end-members may suggest a mixture of dominantly five-fold coordinated iron^{3+} and five- to six-fold coordinated Fe^{2+}. The higher intensity of the dry glasses may indicate higher amounts of low coordinated iron in these glasses. This would be consistent with the previously observed differences in the Mössbauer hyperfine parameters between dry and hydrous glass of the haplotonalitic samples (Wilke et al., 2002). The considerably lower pre-edge intensity of the hydrous haplotonalitic samples synthesized at the most oxidizing conditions and the one that was slowly quenched indicates a change in the average iron site-symmetry towards a higher amount of sites with centrosymmetry. This may indicate the presence of a higher amount of octahedrally coordinated iron in these samples.

The fact that the pre-edge intensity of the two hydrous haplogranitic samples is almost the same despite the difference in the pre-edge centroid also may indicate a difference in iron coordination geometry for at least one of the two iron species. This is also apparent by the difference of the intensity at the shoulder around 7111.5 eV of the fitted pre-edge (Fig.

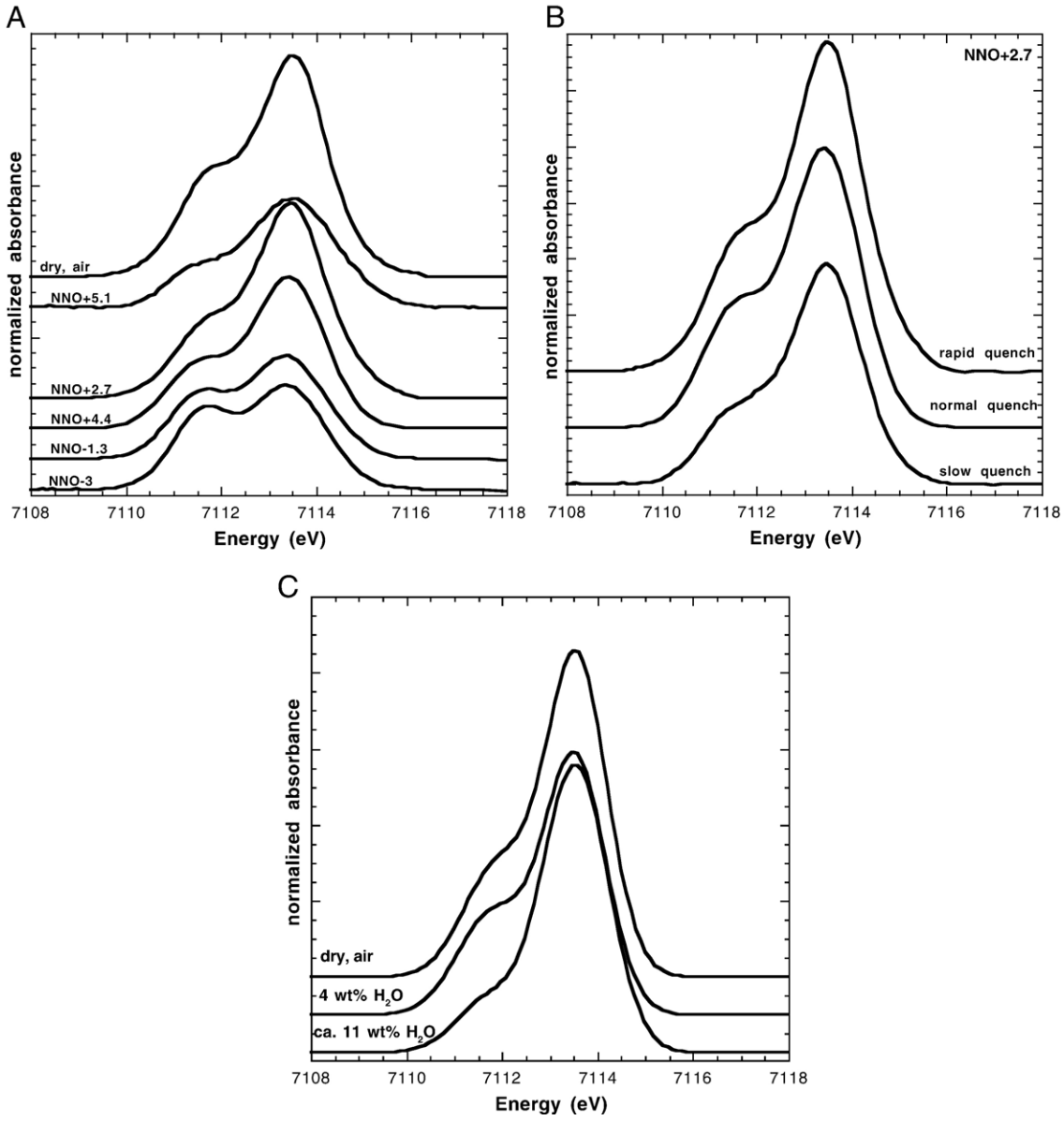

Fig. 3. (A) Pre-edges corresponding to XANES spectra of haplotonalitic samples shown in Fig. 2A resulting from fits of the pre-edge region of the XANES. (B) Pre-edges corresponding to XANES spectra of haplotonalitic samples shown in Fig. 2B. (C) Pre-edges corresponding to XANES spectra of haplogranitic samples shown in Fig. 2C.

3B), which is related to the contribution by Fe^{2+}. The lower intensity at this position for the water-saturated glass may indicate a more centrosymmetric average site geometry for Fe^{2+} in this sample.

3.3. Transmission electron microscopy of haplotonalitic glasses

All glasses have shown no evidence for crystallization by methods like polarization microscopy, X-ray diffraction or electron microprobe. In order to further confirm the lack of crystals in the synthesized samples, four samples of the haplotonalitic glasses synthesized at intrinsic conditions covering the whole range of quench rates used were investigated using TEM. Glasses that were quenched by the normal quench rate or faster display a homogenous amorphous phase. In the slowly quenched sample, tiny crystals are observed in addition to a homogenous amorphous phase. Two TEM samples were prepared from this glass. In one sample, few

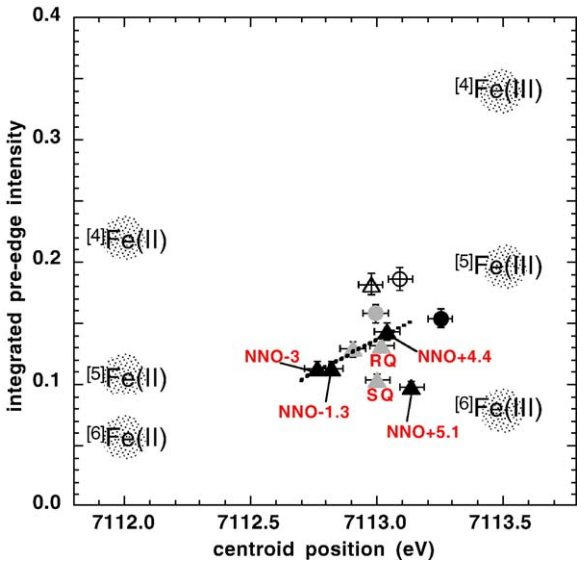

Fig. 4. Integrated pre-edge intensity plotted vs. centroid position of pre-edge of all samples. Grey fields designate pre-edge parameters for the iron coordination and oxidation state indicated derived from crystalline model compounds (Wilke et al., 2001, 2004). Triangles: haplotonalitic samples, open symbols: dry samples, black symbols: hydrous symbols at the redox conditions indicated, grey symbols: hydrous samples at intrinsic conditions (NNO+2.7), (RQ) rapid quench, (SQ) slow quench, (no indicator) normal quench. Circles: haplogranitic samples, open symbols: dry sample, grey symbol: 4 wt.% water, black symbol: water-saturated sample (ca. 11 wt.% water). Dashed line indicates trend of hydrous haplotonalitic samples discussed in text.

crystals with a diameter of 60–400 nm and in the other many crystals bigger in diameter (500 to 1500 nm) were observed and analyzed (Fig. 5). Thus, this slowly

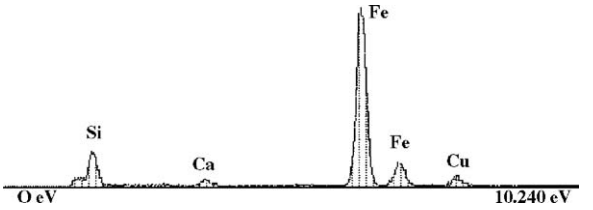

Fig. 6. Typical EDX spectrum of crystals observed in the slowly quenched sample. This particular spectrum was taken on the maghemite shown in Fig. 5. Copper peak is from the sample holder.

quenched glass is characterized by a heterogeneous distribution of the crystallized phases. The EDX analysis shows that all crystals are iron-rich (see for example the EDX spectrum given in Fig. 6) compared to the glass. Based on these EDX spectra and selected area electron diffraction (SAED) patterns, we identify at least three different iron-bearing phases in this sample. Several SAED could be identified as maghemite, γ-Fe_2O_3, or magnetite, Fe_3O_4. As the crystallographic properties of these two phases are very close, it is not always obvious to see the differences between the space group $P2_13$ of maghemite and the space group $Fd3m$ of magnetite. Yet, as shown in Fig. 5, it is possible to make the difference between maghemite and magnetite because the (543) reflection is forbidden in magnetite. Another example is shown in Fig. 5, where only one SAED could be acquired: indexing of the SAED is correct with exactly the same zone axis for maghemite and magnetite. Hence, it cannot be excluded that both types of crystals might be present in the sample. The

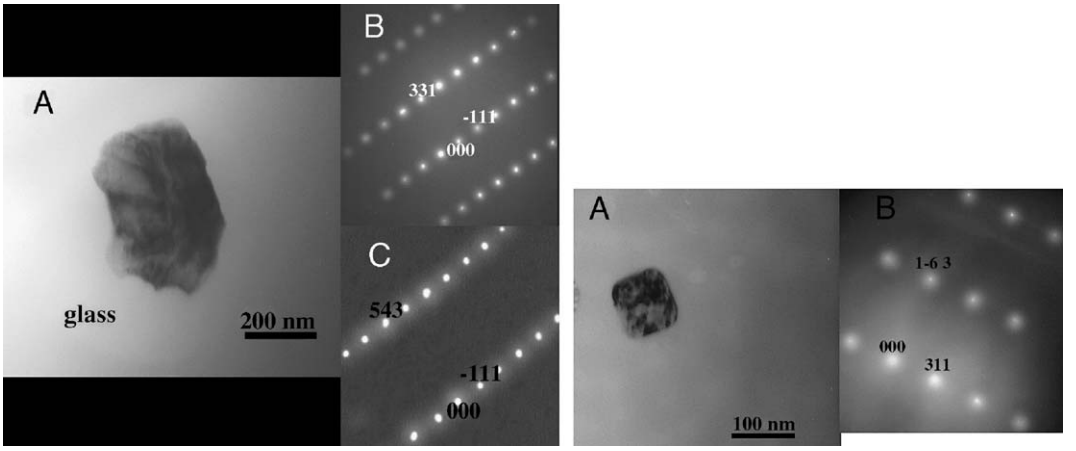

Fig. 5. TEM micrographs and associated selected area diffraction pattern of the slowly quenched sample: left: (A) crystal of maghemite in glassy matrix. Diffraction patterns (B) on [−2 4 0] zone axis and (C) on [−1 2 −9] zone axis coming from the left area of the picture is consistent with the cubic space group $P2_13$ and unit cell parameters for maghemite: a=8.36(10) Å. These patterns are not compatible with other Fe-oxides, even with magnetite as the (543) peak is forbidden. Right: (A) crystal in glassy matrix. (B) The SAED on [−2 4 0] zone axis from the left area of the picture is consistent with the cubic space group $P2_13$ and unit cell parameters a=8.35(10) Å for maghemite or with the cubic space group $Fd3m$ and unit cell parameters a=8.38(10) Å for magnetite.

third type of crystal could not unequivocally be identified.

3.4. EXAFS of haplotonalitic glasses

EXAFS spectra of haplotonalitic samples taken on hydrous glasses synthesized at intrinsic redox conditions (NNO+2.7, rapid, normal and slow quench) and at NNO+4.4 are shown in Fig. 7A. The Fourier-transform (FT) of these spectra is shown in Fig. 7B in comparison to FT of EXAFS spectra taken on model compounds for Fe^{2+} in octahedral, trigonal-pyramidal and tetrahedral and Fe^{3+} in tetrahedral coordination environments. The first peak of the FT, which is related to the Fe–O pair distribution, of all glasses except the slowly quenched one is centred about the harmonic position of $^{[4]}Fe^{2+}$. This, however, has no meaning since all of these glasses contain substantial but comparable amounts of Fe^{3+} (Table 2) on one hand and in addition the EXAFS spectra are probably highly affected by disorder-induced anharmonicity that leads to systematic underestimation of distances if the FT is directly compared to the FT of model compounds (Brown et al., 1995; Farges and Brown, 1996). The slowly quenched glass shows some evident differences in the EXAFS that are mainly expressed in a higher intensity of the second maximum of the FT. In addition, the first maximum of the FT shows a split maximum.

A more evident difference between the three samples with the different quench rates is observed by comparing the FT of EXAFS spectra that were acquired at 77 K (Fig. 7C). In case of the regularly quenched sample appearance of a side lobe around 1.8 Å in the FT of the low-temperature spectrum and an increase of the second maximum are observed, whereas only minor differences are found between the two spectra of the rapidly quenched sample. The reduction of thermally induced disorder at such low temperatures especially enhances contributions to the spectra that stem from iron-sites that are less affected by static disorder. Thus, the temperature-dependent changes in the regularly quenched sample indicate a slightly higher amount of iron-moieties in a more ordered environment. The significant increase of maxima in the FT of the low-temperature spectrum of the slowly quenched sample underpins the presence of iron in a mostly crystalline environment as already proven by the TEM measurements.

We have estimated structural parameters for these samples by fitting of the room temperature EXAFS spectra to better evaluate any differences. The fit was performed considering Fe–O and Fe–Si pairs using an analytical asymmetric pair distribution, which is based on a sum of weighted exponentials (XAFS Software, Winterer, 1996). Phase shift and backscattering amplitude for Fe–O and Fe–Si pairs were extracted from an experimental spectrum of gillespite ($BaFeSi_4O_{10}$). Fitted distances for Fe–O were validated by tests on $FePO_4$ (berlinite structure, tetrahedral Fe^{3+}), grandidierite (trigonal-dipyramidal Fe^{2+}), siderite and fayalite (octahedral Fe^{2+}, regular and distorted). Except for fayalite, the Fe–O distance of the models could be reproduced within 0.01 Å. For the distorted octahedral environment of iron in fayalite, the average Fe–O distance of 2.16 Å (Smyth, 1975) was underestimated by 0.03–0.04 Å, i.e., the two axial oxygens at 2.22 Å are not adequately fitted. This means that contributions of very long Fe–O distances are probably underestimated by the analysis presented here.

The resulting fits of the glass samples are shown in Fig. 7A and fitted parameters are given in Table 3. The parameters fitted from these spectra should be treated with caution for two reasons: (i) the samples are mixed in respect to iron oxidation state ($Fe^{3+}/\sum Fe \approx 0.2–0.3$) and (ii) iron in these samples might reside in more than one phase. Thus, the parameters provide only an average image of the iron environment and are only used here to compare these samples that are similar in oxidation state and to point out features that might indicate ordering around iron or even onset of crystallization. For the rapidly quenched sample, a centroid for the distribution of Fe–O pairs at 2.11±0.04 Å with an average coordination of about 5±1 was determined. For the regularly quenched sample, 6±1 nearest oxygen neighbours at a somewhat larger distance (centroid at 2.14±0.04 Å) are found. The difference is probably not significant given the errors. For both samples, a quite large asymmetry parameter of 0.14±0.02 is fitted, which describes the deviation from a symmetric Gaussian pair distribution, indicating a considerably asymmetric Fe–O pair distribution. A significant

Fig. 7. (A) Normalized k^3-weighted EXAFS ($\chi(k)$) of haplotonalitic samples. Shown are spectra of the hydrous samples synthesized at NNO+4.4 and under intrinsic redox conditions (NNO+2.7) with variable quench rates as indicated. (B) Fourier-transforms (FT) of the k^3-weighted EXAFS (not corrected for phase shift) of the spectra shown in (A). FT of model compounds with Fe^{2+} and Fe^{3+} in various coordinations as indicated. (C) Comparison of the FT of spectra taken at room temperature and at 77 K for the samples indicated. (D) Fourier-filtered $\chi(k)$ of the slowly quenched sample that corresponds to the split first maximum of the FT in (B). Solid thin line: signal of first maximum, window for inverse Fourier-transform: 0.77–1.45 Å; dashed thin line: signal of first maximum, window for inverse Fourier-transform: 1.60–2.10 Å; solid thick line: sum of the former two. (E) Histogram of the reconstructed Fe–O pair distribution function for the slowly quenched sample.

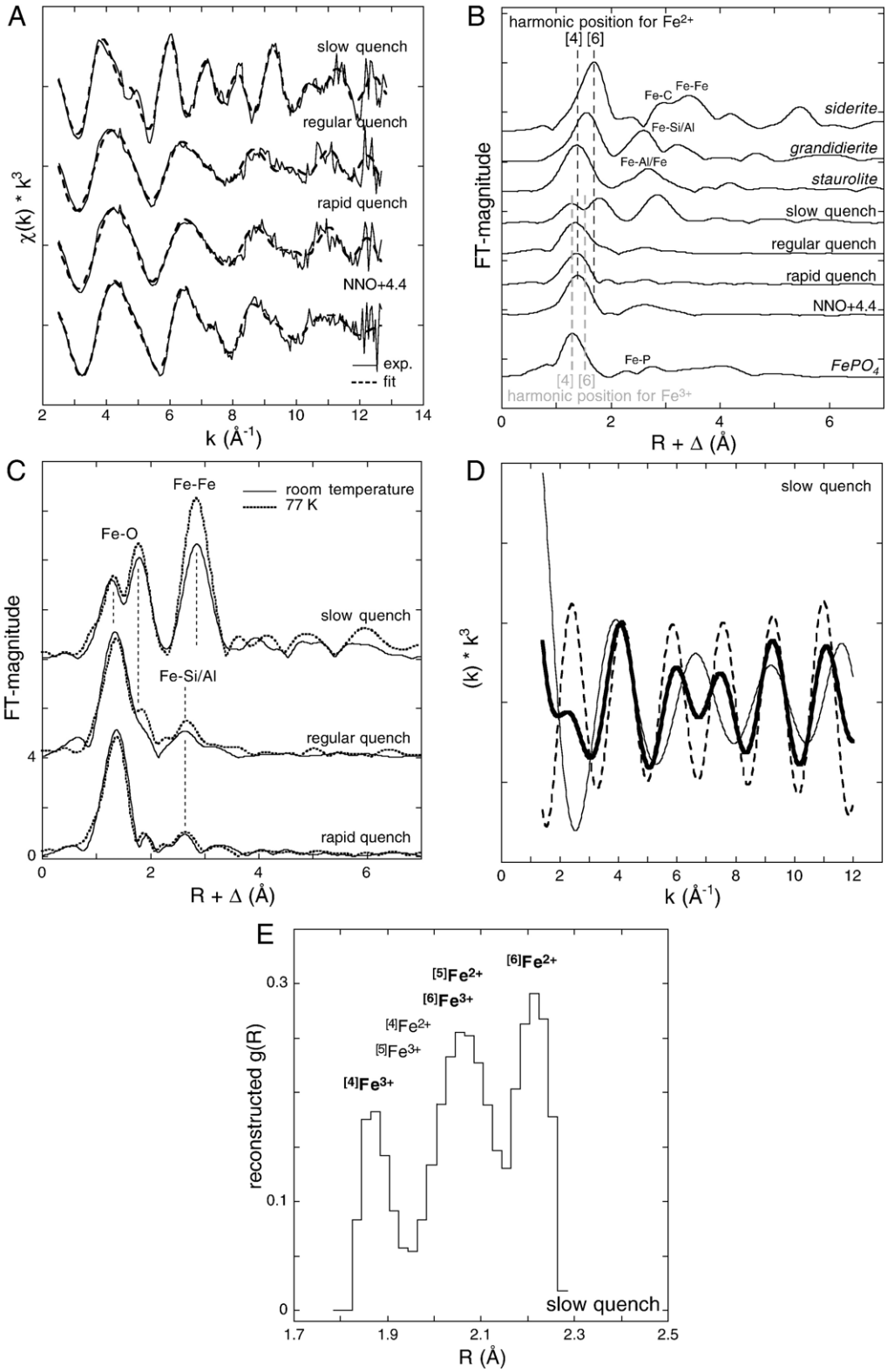
A
slow quench
regular quench
rapid quench
NNO+4.4
exp.
fit
χ(k) * k3
k (Å-1)
B
harmonic position for Fe2+
[4] [6]
Fe-C
Fe-Fe
Fe-Si/Al
Fe-Al/Fe
siderite
grandidierite
staurolite
slow quench
regular quench
rapid quench
NNO+4.4
Fe-P
FePO4
[4] [6]
harmonic position for Fe3+
FT-magnitude
R + Δ (Å)
C
Fe-Fe
room temperature
77 K
Fe-O
slow quench
Fe-Si/Al
regular quench
rapid quench
FT-magnitude
R + Δ (Å)
D
slow quench
(k) * k3
k (Å-1)
E
[6]Fe2+
[5]Fe2+
[6]Fe3+
[4]Fe2+
[5]Fe3+
[4]Fe3+
reconstructed g(R)
slow quench
R (Å)

Table 3
Fitted centroid (R), number of neighbours (N) and relative Debye–Waller factors (σ^2) using Fe–O and Fe–Si pair distributions determined from the EXAFS spectra

Sample, fO_2	R (Å), Fe–O	N, Fe–O	σ^2 (Å^2)[a], Fe–O	Asymmetry	R (Å), Fe–Si	N, Fe–Si	σ^2 (Å^2)[a], Fe–Si	Asymmetry
Haplotonalite								
Hydrous, NNO+4.4	2.05(2)	4.8(7)	−0.002(1)	0.11(1)	3.4(2)	2.2(5)	0.004(2)	0[b]
Hydrous, NNO+2.7, NQ	2.14(4)	6(1)	−0.002(2)	0.14(2)	3.5(2)	1.7(8)	−0.01(1)	0.11(1)
Hydrous, NNO+2.7, RQ	2.11(4)	5(1)	−0.003(2)	0.14(2)	3.5(2)	1.0(5)	−0.01(1)	0.11(1)

[a] Relative to gillespite.
[b] Additional contribution of Fe–Fe distribution was fitted.

contribution to this large asymmetry stems certainly from the fact that both iron oxidation states, and thus very different Fe–O distances, are present in the samples. For the sample synthesized at NNO+4.4, a shorter Fe–O distance is fitted (2.05±0.02 Å) with 4.8±0.8 neighbours and a slightly smaller asymmetry parameter (0.11). In the fit of this sample, an additional contribution by Fe–Fe pairs in the second coordination shell has to be taken into account at 3.21±0.03 Å to model the feature present in the EXAFS at 7.35 Å^{-1}. The presence of this feature may indicate contributions by iron-moieties in a higher ordered environment.

As described above, the slowly quenched glass shows strong differences in the EXAFS compared to the other samples. Calculation of a mix of spectra from magnetite (as indicated by the TEM results) and the regularly quenched sample does not reproduce the spectral features found. Such a split maximum in the FT can be probably explained by destructive interference of the EXAFS signals of Fe^{3+} and Fe^{2+} with very similar Fe–O distances. E.g., this would be the case for $^{[4]}Fe^{2+}$ and $^{[6]}Fe^{3+}$. The destructive interference can be visualized by looking at the Fourier-filtered signal corresponding to the low-distance and high-distance maximum of the first peak in the FT, respectively (Fig. 7D). Destructive interference leads to the "beats" in the EXAFS observed at 2.5 Å^{-1} and 6.8 Å^{-1}. Mustre de Leon et al. (1992) described a similar EXAFS for Cu–O pair distributions in $YBa_2Cu_3O_7$, which could be related to a split position of the oxygen in the Cu–O coordination shell. In case of our sample, the destructive interference is related to the presence of iron in both oxidation states and several different phases in the sample. The EXAFS spectrum could not be fitted by the approach used for the other samples. The Fe–O pair distribution in this sample was reconstructed using a numerical histogram fit to the Fourier-filtered EXAFS related to the Fe–O pair distribution that uses a set of 25 distances to describe this distribution (XAFS-software, Winterer, 1996). A histogram plot describing the contribution of each of the 25 distances to the pair distribution function is shown in Fig. 7E and evidences the complex mixture of iron species present in the sample. In addition, strong contributions by Fe–Fe pairs at a distance of ca. 3.3 Å are found in the EXAFS related to the shell of the next-nearest neighbours that are responsible for the strong second maximum of the FT.

3.5. In-situ XANES of hydrous melt

The observations made on the glass samples provide significant evidence that there is quite some difference in the local structural environment around iron between hydrous and dry glasses. The data collected, so far, indicate already that the structural differences might be related to the quench process and probably do not represent any differences in the iron coordination between dry and hydrous systems present in the melt above T_g. A final evidence for this hypothesis can be found by measurements at in-situ conditions.

Fig. 8 summarizes the XANES measurements on hydrous haplogranitic melt using a HDAC. The spectrum of the starting glass represents the same sample as the water-saturated glass shown in Fig. 2C, only measured inside the HDAC just before the run. In comparison to this, the spectrum taken at 700 °C and 500 MPa is shown. The edge position is shifted to lower energies and the pre-edge peak height is significantly reduced as compared to the glass spectrum. Both changes are owed to the complete reduction of any Fe^{3+} present to Fe^{2+} due to the reducing conditions inside the cell. Beside this, the spectrum reveals a broad structure at the main crest of the edge. The smaller pre-edge intensity is consistent with only Fe^{2+} present in the melt. The spectrum shown is based on an average of 16 scans collected over 6.5 h, after an initial equilibration period. Inspection of single scans revealed that no difference in the spectra is observed after an equilibration period of 1 h.

After lowering of the temperature to 620 °C and 410 MPa, the spectrum changes rapidly and shows a significant narrowing at position A and a shoulder at

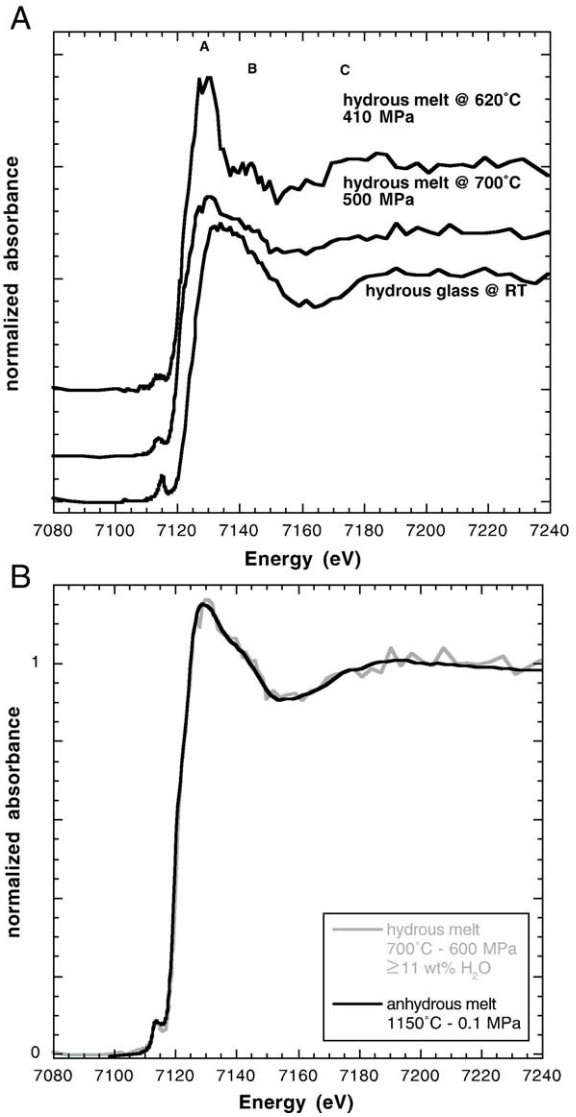

Fig. 8. (A) Normalized XANES of Fe in hydrous haplogranitic glass and melt collected inside the HDAC at temperature and pressure indicated. (B) Comparison of XANES spectra of Fe in dry and hydrous melt collected under in-situ conditions as indicated.

position B of the spectrum. Taken spectra did not change significantly for scans taken 30 min after reaching 620 °C. The spectrum shown is based on three scans acquired over 1 h after these initial 30 min.

The quality of the in-situ spectrum taken at 700 °C in the HDAC does not permit any further detailed analysis of the spectrum taken on the hydrous melt. However, this spectrum can be directly compared to a spectrum that was collected on a dry haplogranitic melt at 1150 °C under reducing conditions (spectrum taken from Wilke et al., in press). Superimposing the two spectra reveals that there is hardly any difference between the two measurements even though the iron content differs (ca. 5 wt.% Fe_2O_3 for the dry sample). This comparison suggests that the structural environment around Fe^{2+} in this kind of melt composition is hardly affected by the dissolution of water in the melt. However, a dry glass may still not be representative for a melt above T_g, as was found in previous studies (Waychunas et al., 1988; Jackson et al., 1993) and is also indicated by new data (Wilke et al., 2004b, in press).

The similarity of dry and hydrous in-situ spectra and the lack of those features observed in the spectra of the hydrous glasses strongly indicates that those spectral features are related to changes in the structural environment of iron occurring during quenching and do not represent the melt above T_g. The features occurring in the spectrum after lowering of the temperature to 620 °C are in principle similar to those observed in the slowly quenched haplotonalitic sample, i.e., narrowing of the maximum at position A, appearance of a shoulder at position B. These changes in the spectra can be related to crystallization of the sample. Growth of crystals can also be observed visually and would be expected from the phase relations for this composition (e.g., Johannes and Holtz, 1996). The nature of these crystals was not further inspected but the quite rapid formation of crystals was also observed during experimental runs at similar P–T conditions during preparation of this in-situ experiment.

To estimate structural parameters of Fe^{2+} in this type of melt composition a Fourier-transform (FT) analysis as suggested by Bugaev et al. (2005) was performed on the XANES spectrum of the dry haplogranitic melt collected at 1150 °C and ambient pressure shown in Fig. 8B. Analysis of the XANES of the hydrous melt was not possible due to the strong noise present in the spectrum. However, resulting parameters of the dry melt are probably transferable to the hydrous melt due to similarity of the two spectra. As suggested by (Bugaev et al., 2005), the FT was applied to the EXAFS part of the XANES over a short range of wave numbers k: 3.6–5.9 $Å^{-1}$ (Fig. 9A). This k-range excludes the main edge crest features and contains only information from the first coordination shell (Bugaev et al., 2005). The fit was performed on the Fourier-filtered signal of the first oxygen shell's peak of the FT (0.3–2.5 Å). Photoelectron phase shift, scattering amplitude and mean free-path length were extracted from an experimental spectrum of gillespite that was treated in the same way as the spectrum of the melt. During fitting, the number of neighbors was fixed to five as found by several

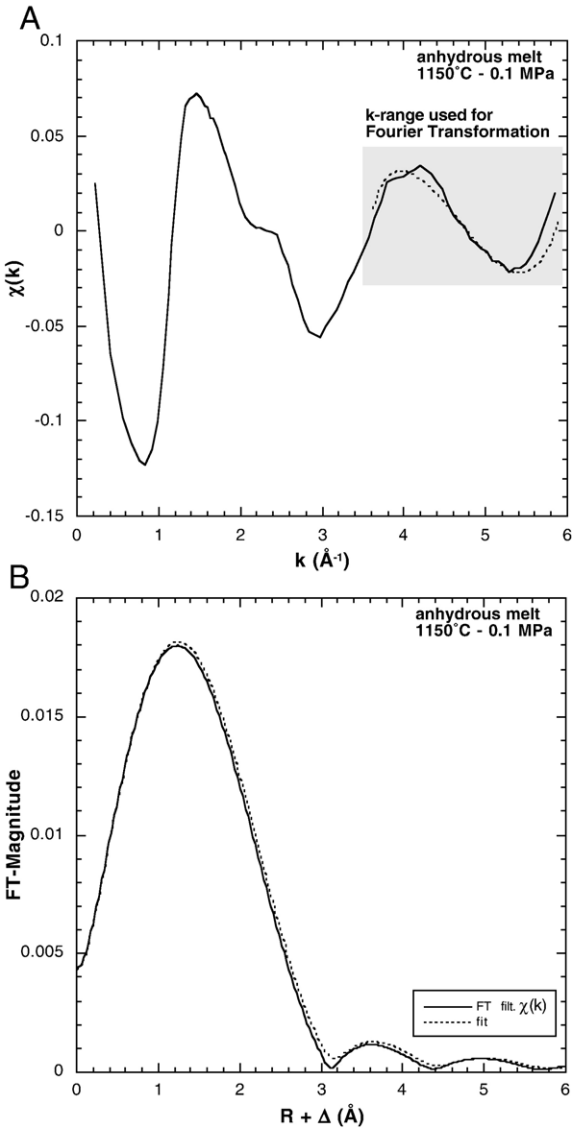

Fig. 9. (A) $\chi(k)$ extracted from the XANES of the dry haplogranitic melt shown in Fig. 8B (solid line) and the Fourier-filtered $\chi(k)$ used for the fit. (B) FT of the filtered $\chi(k)$ and the result of the fit.

authors for Fe^{2+} in silicate glasses (e.g., Rossano et al., 2000; Farges et al., 2004; Bugaev et al., 2005). This had to be done since the number of neighbors and the fitted Debye–Waller factor (σ^2) were strongly correlated during fitting, which led to physically meaningless values. Fig. 9B shows a comparison of the FT of the extracted $\chi(k)$ and the fit. The resulting Fe–O distance $R=2.0\pm0.2$ ($\sigma^2=0.01$ Å^2, rel. to gillespite), which should be considered as an estimate due to the restricted data range, compares well to the values determined by Bugaev et al. (2005) and Rossano et al. (2000) for Fe^{2+} in silicate glass.

4. Implications

In a completely amorphous matrix lacking any long-range order no or very little contribution from next nearest or higher coordination shells of the absorbing atom should be visible in the XANES region of the spectrum. The dry glasses, presented here, show such spectra exhibiting a broad main edge crest followed by the first EXAFS maximum. However, all hydrous glasses exhibit a fine structure at the main crest that is lacking in the dry counterpart. Such spectral features are only possible if at least the medium-range environment of the absorbing atom shows some considerable amount of ordering. The parameters fitted from the EXAFS indicate considerably asymmetric Fe–O pair distributions for the regularly and rapidly quenched samples. Only slight, probably not significant differences between these samples can be detected in the parameters fitted for the oxygen coordination shell. Evidence in the EXAFS of one regularly quenched sample (NNO+4.4) for contributions by iron-moieties in a more ordered environment is provided by the detection of contributions by Fe–Fe pair distributions in the second coordination shell. Still, all glasses quenched by the regular or rapid procedure have shown no evidence for crystallization by other analytical methods like polarization microscopy, X-ray diffraction, Mössbauer spectroscopy and, particularly, TEM. In an analogue study on nickel in hydrous glass, the observed spectral changes upon dissolution of water were much stronger and were present in all glasses containing more than 4 wt.% water, independent of the used quench rate (Farges et al., 2001). The authors could show by TEM investigations the presence of nanocrystalline domains (20–50 Å diameter) of a nepouite-like phase even in rapidly quenched hydrous glasses. In the light of these results for nickel, especially the TEM results, it can be concluded that the scale of ordering around iron in these glasses is still rather restricted to the short-range scale, or at least considerably smaller than the 40 Å determined for the ordered domains around nickel.

The in-situ measurements presented here as well as those presented for nickel in hydrous melts (Muñoz et al., 2005) highlight that the structure found in the hydrous glasses represents the structure of the liquid frozen-in near T_g and differs from the one that can be observed at higher temperatures. As far as it can be ruled out from the rather limited in-situ data presented here, there is no major difference between dry and hydrous melts in the local structural environment of iron for these aluminosilicate compositions. The average Fe–O distance estimated is consistent with Fe^{2+} in an average

coordination between four and five as proposed previously for Fe^{2+} in silicate glass (Rossano et al., 2000; Galoisy et al., 2001; Farges et al., 2004; Jackson et al., 2005).

Differences between glass and melt are related to relaxation or even crystallization processes occurring in the supercooled liquid or around T_g. The efficiency of these processes is dependant on the quench rate in the temperature region of T_g. Since the T_g for the water-saturated glasses is relatively low (T_g for the haplotonalitic glass is estimated to be around 300 °C based on viscosity data by Schulze, 2000), the structure of the liquid cannot be quenched sufficiently in the devices used for synthesis. However, the study of Farges et al. (2001) shows that these ordering/crystallization processes not necessarily affect the bulk of the sample. Instead, they can be restricted to just a few components of the melt such as iron or nickel. For example, some of the nickel-bearing glasses used by Farges et al. (2001) also contained zirconium and no evidence for any ordering or crystallization was found in XAFS spectra of zirconium in dry and hydrous glasses (Farges and Rossano, 2000). Generally, the potential for differences between glass and melt in the coordination of elements in silicate compounds should decrease with the field strength of a given ion present in the melt/glass (Farges and Brown, 1996).

Acknowledgements

We thank R. Schulz, M. Kreplin and the staff of the high-pressure workshop of the GFZ Potsdam as well as D. Vollmer and C. Fischer (Universität Potsdam) for their technical help and support. The support during high-pressure syntheses by the people from the Institut für Mineralogie (Hannover) is also highly appreciated. Help and support during beam time were provided by E. Welter, K. Attenkofer (HASYLAB), M. Borchert (Universität Potsdam), G.M. Partzsch, R. Bernhardt (Universität Heidelberg) M. Munoz, M. Harfouche (Universite Marne-la-vallee) and the staff of ID 22 (ESRF). This study was supported by the Deutsche Forschungsgemeinschaft (DFG) through projects Wi-2000/1-1 and Wi-2000/1-2, and through the DAAD-EGIDE PROCOPE program. **[RR] [JS]**

References

Bajt, S., Sutton, S.R., Delany, J.S., 1994. X-ray microprobe analysis of iron oxidation states in silicates and oxides using X-ray absorption near edge structure (XANES). Geochim. Cosmochim. Acta 58, 5209–5214.

Baker, L.L., Rutherford, M.J., 1996. The effect of dissolved water on the oxidation state of silicic melts. Geochim. Cosmochim. Acta 60, 2179–2187.

Basset, W.A., Shen, A.H., Bucknum, M., Chou, I.M., 1993. A new diamond anvil cell for hydrothermal studies to 2.5 GPa and from −190 to 1200 °C. Rev. Sci. Instrum. 64, 2340–2345.

Basset, W.A., Anderson, A.J., Mayanovic, R.A., Chou, I.M., 2000. Modified hydrothermal diamond anvil cells for XAFS analyses of elements with low energy absorption edges in aqueous solutions at sub- and supercritical conditions. Z. Kristallogr. 215, 711–717.

Berry, A.J., O'Neill, H.S.C., Jayasuriya, K.D., Campbell, S.J., Foran, G.J., 2003. XANES calibrations for the oxidation state of iron in a silicate glass. Am. Mineral. 88, 967–977.

Bonnin-Mosbah, M., Simionovici, A.S., Métrich, N., Duraud, J.-P., Massare, D., Dillmann, P., 2001. Iron oxidation state in silicate glass fragments and glass inclusions with a XANES microprobe. J. Non-Cryst. Solids 288, 103–113.

Borisov, A.A., Shapkin, A.I., 1990. A new empirical equation rating Fe^{3+}/Fe^{2+} in magmas to their composition, oxygen fugacity, and temperature. Geochem. Int. 27, 111–116.

Botcharnikov, R., Koepke, J., Holtz, F., McCammon, C., Wilke, M., 2005. The effect of water activity on the oxidation and structural state of Fe in a ferro-basaltic melt. Geochim. Cosmochim. Acta 69, 5071–5085.

Brown Jr., G.E., Farges, F., Calas, G., 1995. X-ray scattering and X-ray spectroscopy studies of silicate melts. In: Stebbins, J.F., McMillan, P.F., Dingwell, D.B. (Eds.), Structure, Dynamics and Properties of Silicate Melts. Reviews in Mineralogy, vol. 32, pp. 317–410.

Bugaev, L., Farges, F., Rusakova, E., Sokolenko, A., Latokha, Y., Avakyan, L., 2005. Fe coordination environment in Fe(II)- and Fe (III)-silicate glasses via the Fourier-transform analysis of Fe K-XANES. Phys. Scr., T 115, 215–217.

Burkhard, D.J.M., 2000. Iron-bearing silicate glasses at ambient conditions. J. Non-Cryst. Solids 275, 175–188.

Calas, G., Petiau, J., 1983. Coordination of iron in oxide glasses through high-resolution K-edge spectra: information from the pre-edge. Solid State Commun. 48, 625–629.

Dyar, M.D., 1985. A review of Mössbauer data on inorganic glasses: the effects of composition on iron valency and coordination. Am. Mineral. 70, 304–316.

Farges, F., Brown Jr., G.E., 1996. An empirical model for the anharmonic analysis of high-temperature XAFS spectra of oxide compounds with applications to the coordination environment of Ni in NiO, γ-Ni_2SiO_4 and Ni-bearing Na-disilicate glass and melt. Chem. Geol. 128, 93–106.

Farges, F., Rossano, S., 2000. Water in Zr-bearing synthetic and natural glasses. Eur. J. Mineral. 12, 1093–1107.

Farges, F., Munoz, M., Siewert, R., Malavergne, V., Brown Jr., G.E., Behrens, H., Nowak, M., Petit, P.E., 2001. Transition elements in water-bearing silicate glasses/melts: Part II. Ni in water-bearing glasses. Geochim. Cosmochim. Acta 65, 1679–1693.

Farges, F., Lefrere, Y., Rossano, S., Berthereau, A., Calas, G., Brown Jr., G.E., 2004. The effect of redox state on the local structural environment of iron in silicate glasses: a combined XAFS spectroscopy, molecular dynamics, and bond valence study. J. Non-Cryst. Solids 344, 176–188.

Farges, F., Rossano, A., Lefrère, Y., Wilke, M., Brown Jr., G.E., 2005. Iron in silicate glasses: a systematic analysis of pre-edge and XANES features. Phys. Scr., T 115, 957–959.

Fudali, R.F., 1965. Oxygen fugacities of basaltic and andesitic magmas. Geochim. Cosmochim. Acta 29, 1063–1075.

Gaillard, F., Scaillet, B., Pichavant, M., Beny, J.M., 2001. The effect of water and fO_2 on the ferric–ferrous ratio of silicic melts. Chem. Geol. 174, 255–273.

Galoisy, L., Calas, G., Arrio, M.A., 2001. High-resolution XANES spectra of iron in minerals and glasses: structural information from the pre-edge region. Chem. Geol. 174, 307–319.

Gauthier, C., Solé, V.A., Signorato, R., Goulon, J., Moguiline, E., 1999. The ESRF beamline ID26: X-ray absorption on ultra dilute sample. J. Synchrotron Radiat. 6, 164–166.

Haar, L., Gallagher, J.S., Kell, G.S., 1984. NBS7NRC Steam Tables: Thermodynamic and Transport Properties and Computer Programs for Vapor and Liquid States of Water in SI Units. Hemisphere Pub. Corp., Washington, D.C. 320 pp.

Holloway, J.R., Blank, J.G., 1994. Application of experimental results to C–O–H species in natural melts. In: Carroll, M.R., Holoway, J.R. (Eds.), Volatiles in Magmas. Reviews in Mineralogy, vol. 30, pp. 187–230.

Holtz, F., Pichavant, M., Barbey, P., Johannes, W., 1992. Effects of H_2O on liquidus phase relations in the haplogranite system at 2 and 5 kbar. Am. Mineral. 77, 1223–1241.

Holtz, F., Behrens, H., Dingwell, D.B., Johannes, W., 1995. Water solubility in haplogranitic melts. Compositional, pressure and temperature dependence. Am. Mineral. 80, 94–108.

Jackson, W.E., Mustre de Leon, J., Brown Jr., G.E., Waychunas, G.A., Conradsen, S.D., Combes, J.M., 1993. High temperature XAS study of Fe_2SiO_4: evidence for reduced coordination of ferrous iron in the liquid. Science 262, 229–233.

Jackson, W.E., Farges, F., Yeager, M., Mabrouk, P.A., Rossano, S., Waychunas, G.A., Solomon, E.A., Brown Jr., G.E., 2005. Multi-spectroscopic study of Fe(II) in silicate glasses: implications for the coordination environment of Fe(II) in silicate melts. Geochim. Cosmochim. Acta 69, 4315–4332.

Johannes, W., Holtz, F., 1996. Petrogenesis and Experimental Petrology of Granitic Rocks. Springer, Berlin. 335 pp.

Johnston, W.D., 1964. Oxidation–reduction equilibria in iron-containing glass. J. Am. Ceram. Soc. 47, 198–201.

Johnston, W.D., 1965. Oxidation–reduction equilibria in molten Na_2O–SiO_2 glass. J. Am. Ceram. Soc. 48, 184–190.

Kilinc, A., Carmichael, I.S.E., Rivers, M.L., Sack, R.O., 1983. The ferric–ferrous ratio of natural silicate liquids equilibrated in air. Contrib. Mineral. Petrol. 83, 136–140.

Kohn, S.C., 2000. The dissolution mechanism of water in silicate melts; a synthesis of recent data. Mineral. Mag. 64, 389–408.

Kohn, S.C., Dupree, R., Smith, M.E., 1989. A multinuclear magnetic resonance study of the structure of hydrous albite glasses. Geochim. Cosmochim. Acta 53, 2925–2935.

Kohn, S.C., Smith, M.E., Van Eck, E.R.H., Dirken, P.J., 1998. Sodium environments in dry and hydrous albite glasses. Improved ^{23}Na solid state NMR data and their implications for water dissolution mechanisms. Geochim. Cosmochim. Acta 62, 79–87.

Kress, V.C., Carmichael, I.S.E., 1991. The compressibility of silicate liquids containing Fe_2O_3 and the effect of composition, temperature, oxygen fugacity and pressure on their redox states. Contrib. Mineral. Petrol. 108, 82–92.

Kümmerlen, J., Merwin, L.H., Sebald, A., Keppler, H., 1992. Structural role of H_2O in sodium silicate glasses—results from ^{29}Si and ^{1}H NMR spectroscopy. J. Phys. Chem. 96, 6405–6410.

Lytle, F.W., Greegor, R.B., Sandstrom, D.R., Marques, D.R., Wong, J., Spiro, C.L., Huffman, G.P., Huggins, F.E., 1984. Measurement of soft X-ray absorption spectra with a fluorescence ion chamber detector. Nucl. Instrum. Methods Phys. Res., Sect. A, Accel. Spectrom. Detect. Assoc. Equip. 226, 542–548.

Malavergne, V., Guyot, F., Peyronneau, J., Poirier, J.P., 1999. High pressure equilibrium of Ni and Co between metal and mantle minerals. Geochim. Cosmochim. Acta 63, 1819–1824.

Moore, G., Righter, K., Carmichael, I.S.E., 1995. The effect of dissolved water on the oxidation state of iron in natural silicate liquids. Contrib. Mineral. Petrol. 120, 170–179.

Muñoz, M., Ménez, B., Bureau, H., Wilke, M., Schmidt, C., Simionivici, A., Somogyi, A., Malavergne, V., Farges, F., 2005. In situ speciation of nickel in hydrous melts exposed to extreme conditions. Phys. Scr., T 115, 921–922.

Mustre de Leon, J., Conradson, S.D., Batistic, I., Bishop, A.R., Raistrick, I.D., Aronson, M.C., Garzon, F.H., 1992. Axial oxygen-centred lattice instabilities in $YBa_2Cu_3O_7$: an application of the analysis of extended X-ray-absorption fine structure in anharmonic systems. Phys. Rev., B 45, 2447–2457.

Mysen, B.O., 1991. Relations between structure, redox equilibria of iron, and properties of magmatic liquids. In: Perchuk, L. L., Kushiro, I. (Eds.), Advances in Physical Chemistry, vol. 9, pp. 41–98.

Mysen, B.O., Virgo, D., 1986. Volatiles in silicate melts: 1. Interaction between OH groups and Si^{4+}, Al^{3+}, Ca^{2+}, Na^{+}, H^{+}. Chem. Geol. 57, 303–331.

Mysen, B.O., Virgo, D., Neumann, E.R., Seifert, F.A., 1985. Redox equilibria and the structural states of ferric and ferrous iron in melts in the system CaO–MgO–Al_2O_3–SiO_2–Fe–O: relationships between redox equilibria, melt structure and liquidus phase equilibria. Am. Mineral. 70, 317–331.

Paul, A., 1990. Oxidation–reduction equilibrium in glass. J. Non-Cryst. Solids 123, 354–362.

Rossano, S., Ramos, A., Delaye, J.-M., Creux, S., Filipponi, A., Brouder, C.H., Calas, G., 2000. EXAFS and molecular dynamics combined study of CaO–Fe0$_{-2}$$SiO_2$ glass. New insights into site significance in silicate glasses. Europhys. Lett. 49, 597–602.

Sack, R.O., Carmichael, I.S.E., Rivers, M., Ghiorso, M.S., 1980. Ferric–ferrous equilibria in natural silicate liquids at 1 bar. Contrib. Mineral. Petrol. 75, 369–376.

Schmidt, C., Rickers, K., 2003. In-situ determination of mineral solubilities in fluids using a hydrothermal diamond-anvil cell and SR-XRF: solubility of AgCl in water. Am. Mineral. 88, 288–292.

Schmidt, B.C., Riemer, T., Kohn, S.C., Behrens, H., Dupree, R., 2000. Different water solubility mechanisms in hydrous glasses along the Qz–Ab join. Geochim. Cosmochim. Acta 64, 513–526.

Schulze, F., 2000. Untersuchung zum Einfluss von Druck und geloesten Wasser auf die Viskositaet silikatischer Schmelzen: Anwendung eines “parallel-plate”-Viskosimeters unter hohen Druecken. PhD Thesis, University of Hannover, Germany.

Smyth, J.R., 1975. High temperature crystal chemistry of fayalite. Am. Mineral. 60, 1092–1097.

Solé, A.V., Gauthier, C., Goulon, J., Natali, F., 1999. Undulator QEXAFS at the ESRF beamline ID26. J. Synchrotron Radiat. 6, 174–175.

Waychunas, G.A., Apted, M.J., Brown Jr., G.E., 1983. X-ray K-edge absorption spectra of Fe minerals and model compounds: near edge structure. Phys. Chem. Miner. 10, 1–9.

Waychunas, G.A., Brown Jr., G.E., Ponader, C.W., Jackson, W.E., 1988. Evidence from X-ray absorption for network-forming Fe^{2+} in molten alkali silicates. Nature 350, 251–253.

Wilke, M., Behrens, H., 1999. The dependence of the partitioning of iron and europium between plagioclase and hydrous tonalitic melt on oxygen fugacity. Contrib. Mineral. Petrol. 137, 102–114.

Wilke, M., Farges, F., Petit, P.E., Brown Jr., G.E., Martin, F., 2001. Oxidation state and coordination of Fe in minerals: an Fe K-XANES spectroscopic study. Am. Mineral. 86, 714–730.

Wilke, M., Behrens, H., Burkhard, D.J.M., Rossano, S., 2002. The oxidation state of iron in silicic melt at 500 MPa water pressure. Chem. Geol. 189, 55–67.

Wilke, M., Partzsch, G.M., Bernhardt, R., Lattard, D., 2004a. Determination of the iron oxidation state in basaltic glasses using XANES at the K-edge. Chem. Geol. 213, 71–87.

Wilke, M., Partzsch, G.M., Farges, F., 2004b. XAFS of iron in silicate melt at high temperature. Lithos 73, 120 (Suppl.).

Wilke, M., Farges, F., Partzsch, G.M., Schmidt, C., Behrens, H., in press. Speciation of iron in silicate glasses and melts by in-situ XANES spectroscopy. Am. Mineral.

Winterer, M., 1996. The XAFS package. Proceedings of the 6th International Conference on X-ray Absorption Fine Structure (XAFS VI, Grenoble), p. 144.

Xue, X.Y., Kanzaki, M., 2004. Dissolution mechanisms of water in depolymerized silicate melts: constraints from H-1 and Si-29 NMR spectroscopy and ab initio calculations. Geochim. Cosmochim. Acta 68, 5027–5057.

Zotov, N., Keppler, H., 1998. The influence of water on the structure of hydrous sodium tetrasilicate glasses. Am. Mineral. 83, 823–834.

Zotov, N., Yanev, Y., Epelbaum, M., Konstantinov, L., 1992. Effect of water on the structure of rhyolite glasses—X-ray diffraction and Raman-spectroscopy studies. J. Non-Cryst. Solids 142, 234–246.